Chapter 3
Medium Energy Ion Scattering

3.1 Introduction

Medium energy ion scattering is a refinement of the perhaps better known technique of Rutherford back scattering but offers improved energy and angular resolution [1-3]. This allows MEIS to achieve much higher depth resolution as well as forming an ideal tool for the study of surface and near surface structure. The technique has been successfully applied to a number of systems [4-18]. MEIS is closely related to the techniques of LEIS and HEIS [1, 3, 19, 20]. In all these techniques energetic ions (in the case of MEIS usually H^+, He^+ or Li^+) are made to impact the surface under investigation and the scattered ions are detected. MEIS has advantages over both LEIS and HEIS when applied to studies of surfaces. The energy of the ions involved (~100 – 500 keV) are lower than those of HEIS (which are typically ≥1 MeV). The main advantage of this is that the shadow cone radius (see below) is larger, and hence the technique is more surface sensitive. The lower energies also allow for improved energy resolution when detecting the scattered ions, which equates to better depth resolution. Despite these differences HEIS and MEIS are extremely similar, and the physics underlying one technique may be applied to the other. LEIS, on the other hand, employs ions of much lower energy (a few keV). LEIS suffers from neutralization effects of the incident ions. Also at such low energies the scattering potential is not well known, unlike the case in MEIS and HEIS. The low energy also makes the technique extremely surface sensitive, which may be advantageous but might also be a hindrance in the study of near surface buried interfaces. LEIS does have the further advantage that it does not require the dedicated facilities necessitated by MEIS and HEIS and can indeed be performed in a standard laboratory.

MEIS also has advantages over other techniques such as LEED, mainly that it produces data in real space. Also, as the scattering is kinematic, the data reflects real atomic positions, which is not necessarily the case with other real space imaging techniques such as STM. MEIS also has the advantage over STM in that it can provide information about relatively deep layers rather than just the surface or very near surface region. If the elements present are separated enough in terms of mass then the ions scattered from each can be resolved. This can greatly aid in the interpretation of the MEIS data as shall be seen in later chapters.

3.2 The Technique of MEIS

As the scattered ions have energies of around 100 keV their speed is much greater than that of the atom's movement due to crystal phonon vibrations, so the ions essentially see a frozen snapshot of the crystal. This allows the scattering to be considered as a sequence of kinematic scattering events between ion and crystal atomic nucleus [3, 19, 21].

3.2.1 Shadowing and Blocking

MEIS generally gains its surface sensitivity from the practice of "shadowing". The ionic beam is aligned along a major crystallographic direction (in practice the crystal is rotated about the beam). This shadows atoms deeper in the crystal, further along the "row", as shown in Figure 3.1.

The shadowed volume forms a cone, the radius of which increases with distance from the shadowing atom. For a Coulomb potential this radius is given by

$$R = 2\sqrt{\frac{Z_1 Z_2 e^2 l}{E}} \tag{3.1}$$

where Z_1 and Z_2 are the atomic numbers of ion and target, E is the ion energy and l is the distance from the atom. While equation 3.1 gives an estimate of the size

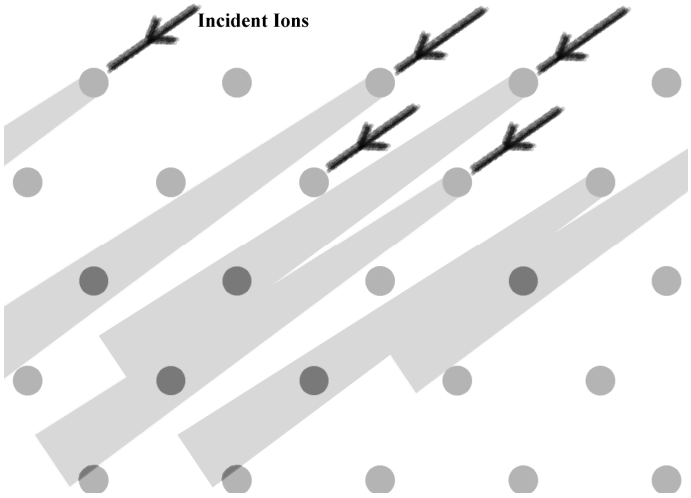

Figure 3.1: Shadowing. By aligning the ion beam along a low index crystallographic direction, the atoms deeper in the crystal are effectively shadowed from the beam.

of the blocking cone it neglects screening of nuclear charge. A more accurate description can be given by the Molière approximation [3, 21]. The radius of the shadow cone then becomes

$$R_M = \xi R \tag{3.2}$$

ξ is the screening potential, which takes a value less than one.

Shadowing has the overall effect that the illumination of the crystal is restricted to a certain depth, although thermal vibrations mean that the shadowing is not ideal and deeper layers do provide some contribution to the backscattered yield. This means that the scattered ions are surface sensitive, with the added advantage that buried interfaces close to the surface can still be probed. Careful selection of scattering geometry can therefore be used to dictate the number of layers exposed.

Although shadowing is useful, further information about the crystal under investigation can be gained by the use of “double alignment”. This essentially uses the same technique as shadowing but to produce blocking of the scattered

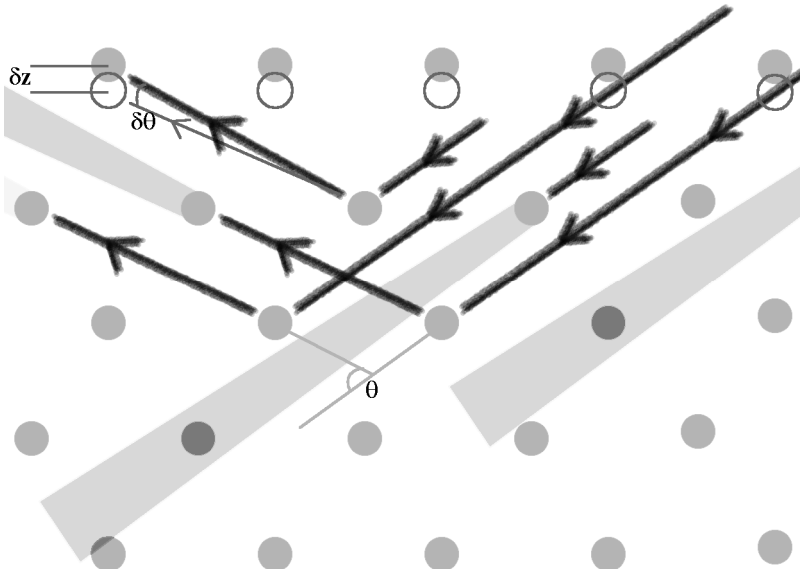

Figure 3.2: Blocking. Scattered ions are blocked in their path back out of the crystal by atoms closer to the surface in a process analogous to the initial blocking. A shift in atomic position results in a shift in the angular position of a blocking feature.

ions (i.e. scattered ions are detected around another low index direction). There is then a drop in scattering yield at characteristic angles where the scattered beamintersects atoms on its way out of the crystal, as demonstrated in Figure 3.2.

A relaxation of the surface layer will then produce a change in the scattering angle of a blocking feature as Figure 3.2 shows. Additional blocking features may also be present due to reduced shadowing of deeper layers. This means that detecting the scattering yield as a function of angle gives real space geometrical information regarding the crystal atomic positions.

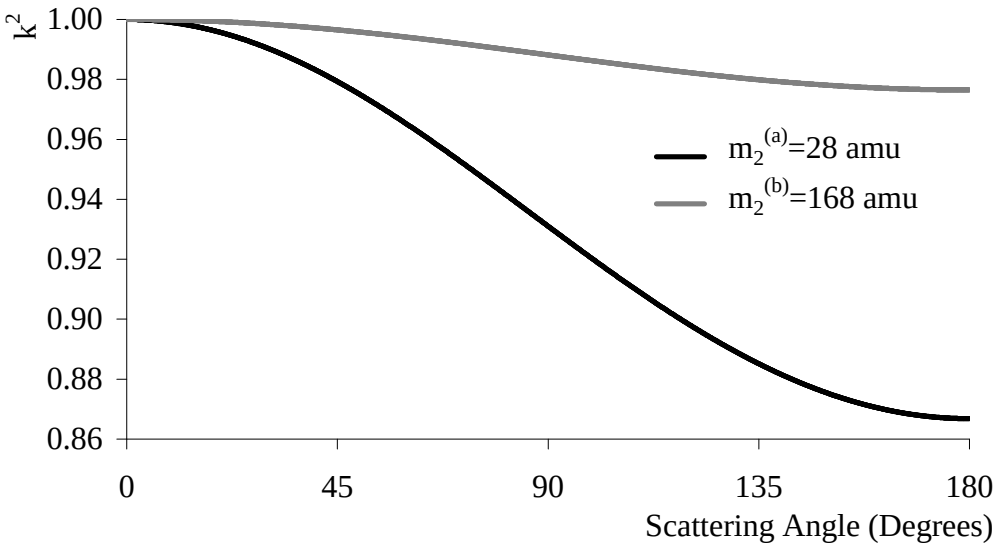

Figure 3.1: The kinematic factor k^2 as a function of scattering angle for two target masses of 28 amu and 168 amu, calculated for the case of H^+ ions.

3.2.2 Kinematic Scattering

As mentioned above, the scattering of the ion from an atomic nucleus within the crystal can be treated as a kinematic event. Considering elastic scattering between two bodies, an ion with initial energy E_0 and mass m_1 scattered from a target of mass m_2 over a scattering angle θ (see Figure 3.2), will scatter with energy given by

$$E = \left[\frac{\left(m_2^2 - m_1^2 \sin^2 \theta\right)^{1/2} + m_1 \cos\theta}{m_1 + m_2} \right]^2 E_0 = k^2 E_0 \qquad (3.3)$$

k^2 is known as the kinetic energy loss factor and it has important consequences for MEIS. A plot of k^2 as a function of scattering angle in the case of H^+ ions is shown in Figure 3.3 for two different target masses, $m_2^{(a)}$ and $m_2^{(b)}$. The kinematic factor for the two target masses becomes increasingly different with increasing scattering angle. In practice this means that for sufficiently high scattering angles MEIS has the power to resolve elements of different mass

Original in colour

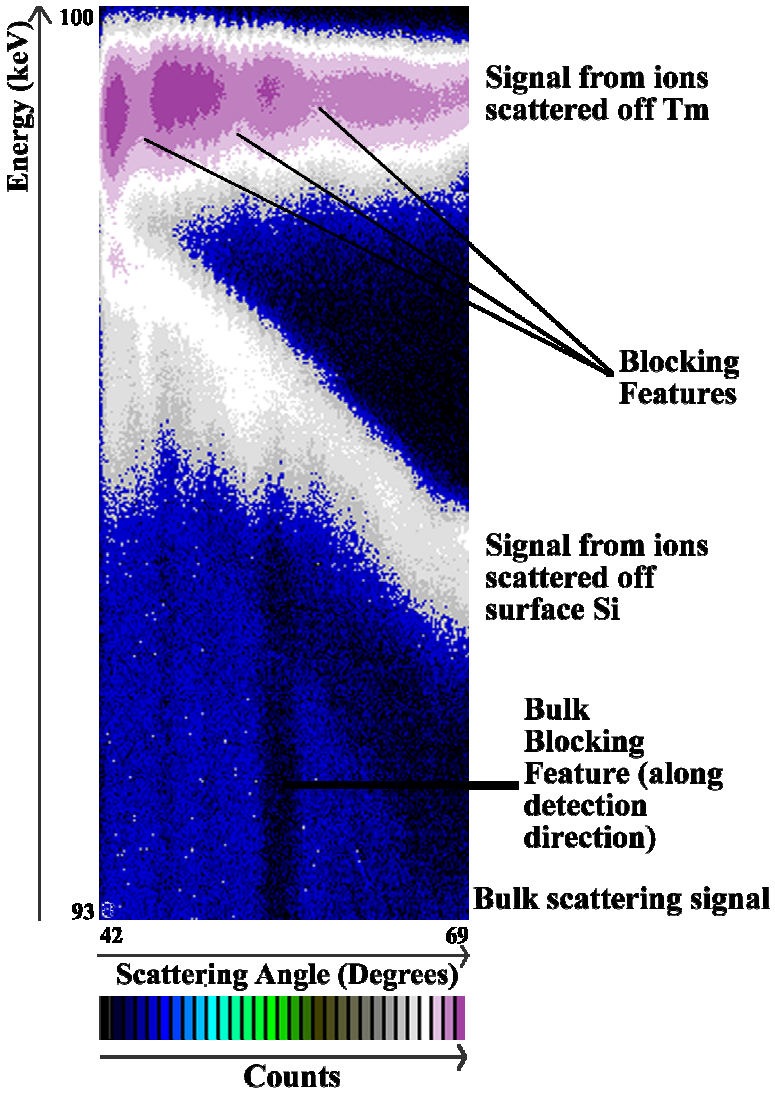

Figure 3.4: An example MEIS spectra (taken from the Tm 2D silicide system, see Chapter 4 for details). This spectrum demonstrates many of the features of a typical MEIS spectrum. The signals from scattering from the Si and Tm are well separated due to the mass difference between the two elements. The Tm scattering signal shows the characteristic fall in counts at increasing scattering angle due to the Rutherford scattering cross-section. The drop in energy with increasing scattering angle is most evident in the Si scattering signal. The Tm scattering signal shows clear evidence of ions being blocked at specific scattering angles. The detection around a major crystallographic direction is evidenced by the bulk blocking feature.

within the crystal. Also, for a given mass, k^2 decreases with increasing scattering angle. This results in ions scattered through higher angles having lower energies. Both of these effects are shown in the example MEIS spectrum, Figure 3.4.

Another factor affecting the scattering data from a MEIS experiment is the fall off in the number of counts with increasing scattering angle. This is a consequence of the Rutherford scattering cross-section, $d\sigma/d\Omega$. The scattered ion flux I over a solid angle $\Delta\Omega$ is given by

$$I = NQ\left(\frac{d\sigma}{d\Omega}\right)\Delta\Omega \tag{3.4}$$

where for the incident ion flux Q, N is the number of atoms contributing to the backscattering. The Rutherford scattering cross-section is given by

$$\frac{d\sigma}{d\Omega} = F\left[\frac{Z_1 Z_2 e^2}{4E\sin^2(\theta/2)}\right]^2 g(\theta, M_1, M_2) \tag{3.5}$$

F is a factor to correct for screening of the target nucleus by electrons, Z_1 and Z_2 are the ion and target atomic numbers, E is the incident energy and $g(\theta, M_1, M_2)$ is a transformation from the centre of mass to laboratory frame.

Equations 3.4 and 3.5 shows that there is a strong dependence in the scattered ion flux with scattering angle. The equations also show that MEIS is more sensitive to heavier elements, as the Rutherford scattering cross-section, and hence detected ion flux, is proportional to the square of the atomic number. Again this can be seen in Figure 3.4.

A final factor when considering MEIS spectra is the energy loss due to inelastic scattering between the ion and electrons. The rate of this energy loss is known as the stopping power. The stopping power depends on the material and the ion energy, which of course decreases due to the inelastic collisions as the ion moves through the crystal. The stopping power is therefore not constant as the ion moves through the sample. However, in MEIS the layers are normally thin

enough and inelastic loses small enough that the stopping power can be taken to be constant before backscattering and then taken to be a different constant after the backscattering event. Taking this surface approximation that backscattering occurs close to the surface and inelastic losses are therefore small,

$$\left(\frac{dE}{dr}\right)_{E_{in}} = \left(\frac{dE}{dr}\right)_{E_0} \tag{3.6}$$

and

$$\left(\frac{dE}{dr}\right)_{E_{out}} = \left(\frac{dE}{dr}\right)_{k^2E_0} \tag{3.7}$$

The inelastic energy loss per unit length normal to the surface is given by

$$\frac{dE}{dz} = \left[\frac{k^2}{\cos\theta_1}\left(\frac{dE}{dr}\right)_{E_0} + \frac{1}{\cos\theta_2}\left(\frac{dE}{dr}\right)_{k^2E_0}\right] \tag{3.8}$$

where θ_1 and θ_2 are as defined in Figure 3.6.

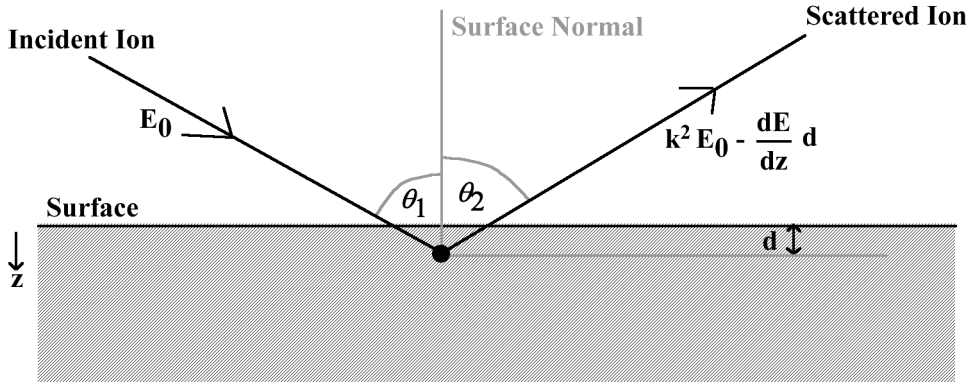

Figure 3.6: The energy loss due to inelastic scattering becomes greater the deeper the ion penetrates. An ion entering the crystal with energy E_0 and being scattered at a depth d from the surface exits with energy given by Equation 3.9.

Therefore the energy of an ion scattered at a depth d will be

$$E = k^2 E_0 - \left[\frac{k^2 d}{\cos\theta_1} \left(\frac{dE}{dr} \right)_{E_0} + \frac{d}{\cos\theta_2} \left(\frac{dE}{dr} \right)_{k^2 E_0} \right] \tag{3.9}$$

Equation 3.9 reveals that the energy scale is therefore a depth scale, as well as being a mass scale due to the elastic scattering. This means MEIS can also be used as a powerful depth profiling technique as well as for structural determination.

MEIS data may therefore be considered in two ways. In the first the data is considered as a function of the energy of the scattered ions integrated over a given angular range. This acts as both a mass and depth scale. Second the data may be considered as a function of angle, the number of counts being integrated over a given energy range. This gives direct geometric information regarding the structure of the surface layers. Within this plot of counts as a function of angle there will be a dip in counts at scattering angles where ions have been blocked by surface atoms. The angular width of these dips is given by [1]:

$$\psi = 2 \left(\frac{nAc}{Es^n} \right)^{1/(n+1)} \left(1 + \frac{1}{n} \right) \text{ radians} \tag{3.10}$$

Here s is the distance between the atom which scattered the ion and the atom which blocked the ion, E is the ion energy given by Equation (3.3), n is the power of the potential, A is the potential parameter and the factor c is given by

$$c = \sqrt{\pi} \frac{\Gamma(1/2n + 1/2)}{\Gamma(1/2n)} \tag{3.11}$$

For a Coulomb potential Equation (3.11) reduces to

$$\psi = 4 \left(\frac{A}{Es} \right)^{1/2} \tag{3.12}$$

$$A = \frac{Z_1 Z_2 e^2}{4\pi\varepsilon_0} \tag{3.13}$$

Therefore the typical width of a blocking dip is a few degrees.

3.3 Simulation of Scattering Curves

Although it is possible to directly interpret MEIS data as described above, for a true quantitative structural analysis it is desirable to simulate the scattering of ions from a number of trial structures and compare these simulations with experiment. If nothing else then simple geometrical considerations, whilst providing a good starting point, neglect the effect of lattice vibrations which may introduce additional scattering as deeper layers are imperfectly shadowed. There may also be edge effects around the shadowing cones which can enhance the scattering yield at particular angles. Monte Carlo simulations are performed using a FORTRAN computer code known as VEGAS, developed by the FOM Institute [2, 19, 21, 22]. A brief description of the method by which the scattering is simulated is given here.

3.3.1 Hitting and Detection Probabilities

As mentioned above, the ions involved in MEIS are travelling with a speed approximately three orders of magnitude faster than the lattice vibrations of the atoms in the crystal, which allows a simple snapshot of the sample to be considered, the atoms “frozen” in their thermally displaced positions. The trajectory of the ion can then be modelled as a series of straight line segments between deflections.

Figure 3.6 below shows the basic double alignment situation. The ion enters the crystal parallel to the z_1-axis and passes a number of atoms before scattering from atom A. It then passes a number of atoms, exiting the crystal parallel to the z_2-axis. Now if the intersection of ion beam and atom A at position $\mathbf{r_a}$ has

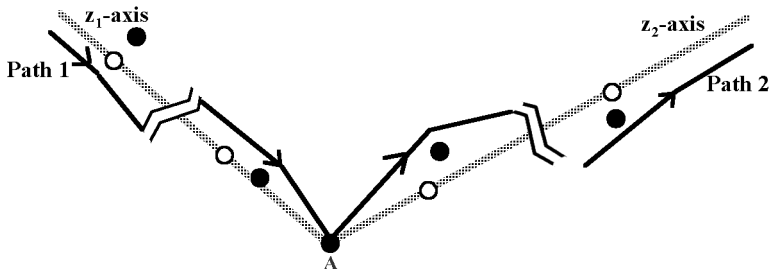

Figure 3.6: Basic double alignment scattering. Open circles indicate equilibrium positions of atoms, filled circles the thermally displaced positions in the crystal snapshot. The ion enters parallel to the z_1-axis, scatters from atom A and exits parallel to the z_2-axis.

probability $P^1(\mathbf{r_a})$, and the probability of the ion being emitted from $\mathbf{r_a}$ and being reaching the detector is $P^2(\mathbf{r_a})$, then the double alignment probability of scattering from atom A at $\mathbf{r_a}$ being detected is given by

$$P_a^{DA} = \int P^1(\mathbf{r_a}) G_a(\mathbf{r_a}) P^2(\mathbf{r_a}) d\mathbf{r_a} \tag{3.14}$$

$G_a(\mathbf{r_a})$ being the Gaussian probability density for the thermal displacement of atom A.

Hitting and detection probabilities are given by

$$P_a^1 = \int P^1(\mathbf{r_a}) G_a(\mathbf{r_a}) d\mathbf{r_a} \tag{3.15}$$

and

$$P_a^2 = \int P^2(\mathbf{r_a}) G_a(\mathbf{r_a}) d\mathbf{r_a} \tag{3.16}$$

respectively. Note that equation (3.16) arises due to the fact that the ion scattering is time reversible. i.e. the probability of detecting the ion scattered from atom A along the z_2-axis is equal to the probability of an ion entering the crystal along the z_2-axis being scattered from atom A.

The double alignment probability can be very well approximated by

$$P_a^{DA} \approx P_a^1 P_a^2 \tag{3.17}$$

The hitting and detection probabilities can therefore be calculated independently and multiplied together to give the total double alignment probability.

3.3.2 Calculation of Probabilities: The Standard Method

Two methods are described in the literature for the calculation of the hitting and detection probabilities [21, 23]. They are shown by Tromp and van der Veen [21] to be equivalent.

Figure 3.7 shows the scheme used in the so called standard method, originally due to Barrett [23]. The ion enters at position $\mathbf{r_0}(\mathbf{x},\mathbf{y})$ and is subsequently scattered by atoms located at $\mathbf{r_1}'$, $\mathbf{r_2}'$, ..., $\mathbf{r_n}'$. A collision occurs if the atom in plane n is located at $\mathbf{r_0} + \mathbf{\Delta n}$. The probability density for such a track through the planes 1,...,n is given by

$$p(\mathbf{r}_0) = G_i(\mathbf{r_0} + \Delta\mathbf{n}) \prod_{j=1}^{n-1} G_j(\mathbf{r_j}') \tag{3.18}$$

Integrating over all possible values of $\mathbf{r_0}$ and sets of $\{\mathbf{r_1}', \mathbf{r_2}', ..., \mathbf{r_{n-1}}'\}$ gives

$$P_n = \int ... \int G_n(\mathbf{r_0} + \Delta\mathbf{n}) \left[\prod_{j=1}^{n-1} G_j(\mathbf{r_0} + \mathbf{r_j}) d\mathbf{r_j} \right] d\mathbf{r_0} \tag{3.19}$$

having substituted $\mathbf{r_j}' = \mathbf{r_0} + \mathbf{r_j}$ and $d\mathbf{r_j}' = d\mathbf{r_j}$ as integration over $\mathbf{r_j}$ is performed at constant $\mathbf{r_0}$.

This integral has 2n integration factors and so must be solved numerically. Random values of $\mathbf{r_0}$ are chosen uniformly from a sufficiently broad area and the $\{\mathbf{r_j}\}$ chosen quasi-randomly from the G_j of the atoms. The track is then

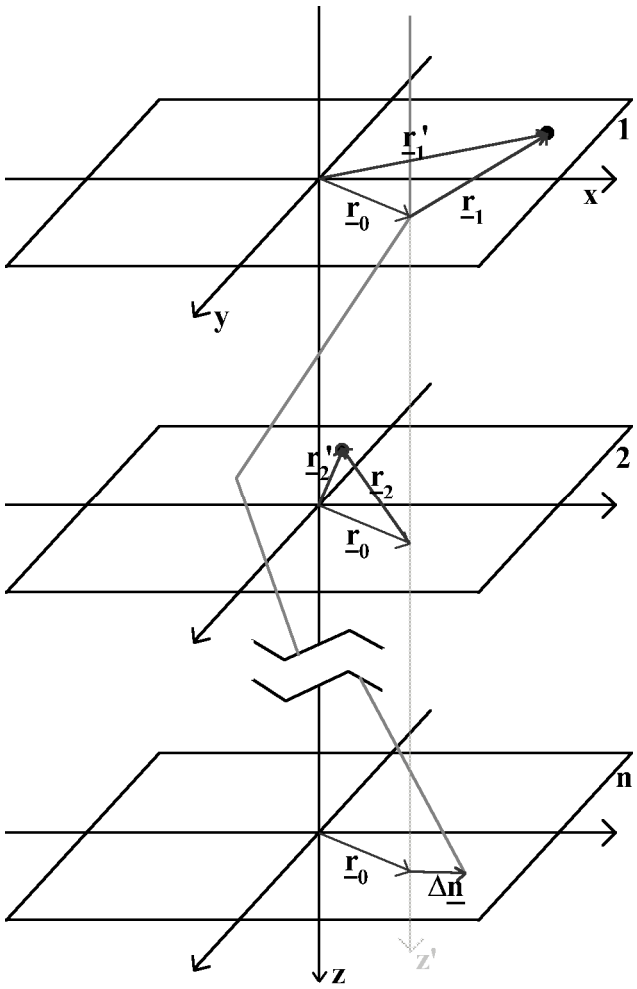

Figure 3.7: Schematic of the standard scheme for determining hitting probabilities. The ion enters at $\mathbf{r_0}$ *and scatters from each atom in turn before colliding with the atom located at* $\mathbf{r_0} + \boldsymbol{\Delta n}$*. Note the z´-axis is the z-axis of the Tromp and van der Veen method.*

calculated and the probability density for a nuclear encounter, $G_n(\mathbf{r_0} + \mathbf{\Delta n})$ is found. This is repeated for many ion tracks to give p_n after appropriate normalisation.

3.3.3 Calculation of Probabilities: Tromp and van der Veen's Method

The method proposed by Tromp and van der Veen [21] is related to that of Barrett by a simple coordinate transformation. There is, however, one important difference. Within the new formalism it is possible to calculate the hitting probabilities of atom i when it is located at a specific $\mathbf{r_i}$, something which is

impossible within the standard formalism. This enables double alignment geometries to be calculated with reasonable efficiency.

Figure 3.8 shows the schematic for the new scheme. The probability that atom i is hit by the ion beam which impinges on the crystal along the z-axis is calculated as follows. The ion is deflected by atoms 1, 2, ..., i-1 at positions {$\mathbf{r_1}$, $\mathbf{r_2}$, ..., $\mathbf{r_{i-1}}$} before passing through the i^{th} plane. In general it will not pass through this plane at $\mathbf{r_i}$ but at a position $\boldsymbol{\delta}\mathbf{r_i}$ away. However, only the coordinates of the atoms relative to the incoming ion beam determine the deflection angles and

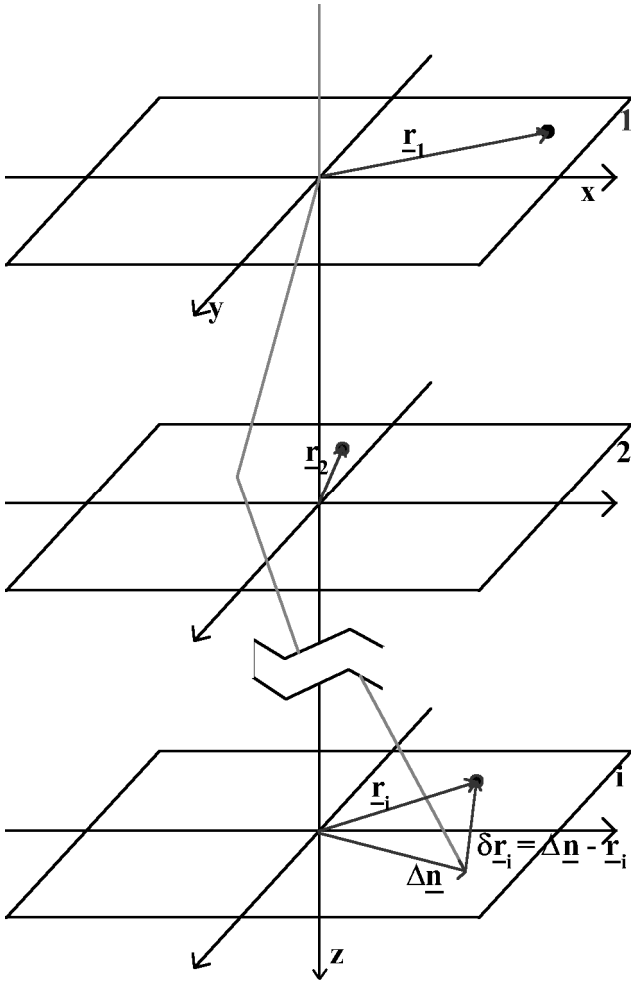

Figure 3.8: Schematic of Tromp and van der Veen's scheme for determining hitting probabilities. The ion enters along the z-axis and is scattered by each atom in turn until passing through the i^{th} layer at $\boldsymbol{\Delta n}$, $\boldsymbol{\delta r_i}$ from the i^{th} atom. This scheme is related to Barrets by a simple coordinate transform (see Figure 3.7).

hence the position at which the beam passes through plane i. If the atoms were located at $\{\mathbf{r_1} - \boldsymbol{\delta}\mathbf{r_i}, \mathbf{r_2} - \boldsymbol{\delta}\mathbf{r_i}, ..., \mathbf{r_{i-1}} - \boldsymbol{\delta}\mathbf{r_i}\}$ and the beam entered the crystal at $-\boldsymbol{\delta}\mathbf{r_i}$ then it would pass through the i^{th} plane at $\mathbf{r_i} + \boldsymbol{\delta}\mathbf{r_i} - \boldsymbol{\delta}\mathbf{r_i} = \mathbf{r_i}$ and a collision would occur.

The probability density for a collision at point $\mathbf{r_i}$ is therefore given by the probability density for the atoms to occupy not $\{\mathbf{r_1}, \mathbf{r_2}, ..., \mathbf{r_{i-1}}\}$ but $\{\mathbf{r_1} - \boldsymbol{\delta}\mathbf{r_i}, \mathbf{r_2} - \boldsymbol{\delta}\mathbf{r_i}, ..., \mathbf{r_{i-1}} - \boldsymbol{\delta}\mathbf{r_i}\}$.

$$p_i = \prod_{j=1}^{i-1} G_j(\mathbf{r_j} - \delta\mathbf{r_i}) \tag{3.20}$$

The probability density of hitting atom i at position $\mathbf{r_i}$ is then the integral over all possible positions of the previous i - 1 atoms

$$P_i(\mathbf{r_i}) = \int \prod_{j=1}^{i-1} G_j(\mathbf{r_j} - \delta\mathbf{r_i}) d\mathbf{r_j} \tag{3.21}$$

The hitting probability of atom i is given by integration over all possible positions of atom i

$$P_i = \int G_i(\mathbf{r_i}) P_i(\mathbf{r_i}) d\mathbf{r_i} \tag{3.22}$$

This can easily be shown to be equivalent to the standard method. Substituting $\mathbf{r_i''} = \mathbf{r_i} - \boldsymbol{\Delta}\mathbf{n} = -\boldsymbol{\delta}\mathbf{r_i}$ into equation (3.21) and using $d\mathbf{r_i''} = d\mathbf{r_i}$ as $\boldsymbol{\Delta}\mathbf{n}$ does not depend on $\mathbf{r_i}$ gives

$$P_i = \int ... \int G_i(\mathbf{r_i''} + \Delta\mathbf{n}) \left[\prod_{j=1}^{i-1} G_j(\mathbf{r_j} + \mathbf{r_i''}) d\mathbf{r_j} \right] d\mathbf{r_i''} \tag{3.23}$$

If $\mathbf{r_i''}$ is renamed $\mathbf{r_0}$ then equation (3.23) is seen to be identical to equation (3.19) under the standard method, and the two formalisms are equivalent.

Again integration is performed by Monte Carlo methods. Uniform random values of $\{\mathbf{r}_1, ..., \mathbf{r}_{i-1}\}$ are chosen and the value of $\mathbf{r}_i$ chosen according to the Gaussian probability distribution. The ion track is determined and the probability densities for the shifted positions found. Averaging over many tracks produces the hitting probability.

3.3.4 Connection of Ingoing and Outgoing Ion Tracks

Equation (3.17) makes the approximation that the incoming and outgoing ion tracks are in fact not correlated. In reality of course there is a correlation, both sharing the same thermally displaced position of the scattering atom. Under normal circumstances this approximation does not cause problems. However, if the hitting probabilities are strongly varying with $\mathbf{r}_a$ for positions close to atom a's equilibrium position, then the approximation may result in a slight shift of the angular position of a blocking minima.

The two tracks may be connected by using a combination of the methods of Barrett and Tromp and van der Veen as described in sections 3.3.1 and 3.3.2 respectively. Barrett's method is used for the calculation of the incoming tracks and then the interception with the final plane is used as the position of the target atom in a calculation for the (time reversed) outgoing track using the method of Tromp and van der Veen, causing the two tracks to intersect. This has the disadvantage that Tromp and van der Veen's method results in a large number of ion tracks with low probability because they must be shifted to intersect the scattering position.

In all the work reported in this thesis, simulations of blocking curves do not have ingoing and outgoing tracks connected. The reasoning behind this is two fold. First it is not expected that any significant error should be introduced by this approximation. The approximation is most likely to fail when the scattering atom lies at the edge of a shadow cone, a situation not encountered in this work. Second, from a practical point of view, the portion of the computer codes which allows such a connection does not correctly function as of this writing, so it is not

possible to specify the connection of ingoing and outgoing tracks within the simulations.

3.3.5 Tracking of Ions: The Single Row Approximation

In order to determine the hitting probabilities the ion track (i.e. the sequence of collisions) must be determined. If the shadow cone radius is suitably small enough that scattering between adjacent rows of atoms plays no role (i.e. the shadow cone is smaller than the distance between rows) then the single row approximation may be employed. The ion path is considered as a sequence of small angle deflections along the atomic row, the order of encounters simply being the order of atoms in the row. If the atomic rows are equivalent then periodic boundary conditions may be used.

The single row approximation fails, however, if the ion can scatter between rows. This may occur, for instance, if the ion beam is not aligned, or aligned along a high index direction. Also surface relaxations can cause adjacent rows to be inequivalent so periodic conditions may no longer be applied.

3.3.6 Tracking of Ions: The Complete Crystal Method

To overcome the shortfalls of the single row approximation the VEGAS codes use the more sophisticated complete crystal method. The complete crystal is treated as a slab of the depth to be considered in scattering, constructed of periodically repeated building blocks which have the lateral dimensions of the $n \times m$ unit cell. If necessary two or more unit cells are combined to get a rectangular building block. The hitting probabilities are calculated as described above. The order of collisions is now lost and must be found for each ion individually.

Whilst in principle it would be possible to determine the next collision partner by calculating the distance from the projected ion trajectory to all atoms within the block, this is prohibitively expensive in computational time. Instead an auxiliary

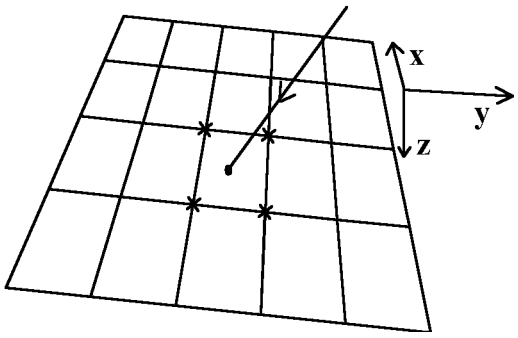

Figure 3.9: In the complete crystal method an auxiliary lattice can be constructed by grouping atoms with (nearly) identical x-, y- or z-coordinates. This can then be used to track the ion through the crystal. As each atom occupies one auxiliary lattice point, and each lattice point contains zero or one atoms, only four auxiliary lattice points need be checked for potential collision partners.

lattice is formed by grouping the atoms within the block into sets with (nearly) identical x-coordinates, (nearly) identical y-coordinates and (nearly) identical z-coordinates. These sets define x-, y- and z-planes, the intersections of which define the points of the rectangular auxiliary lattice. Each auxiliary lattice point is either empty or contains exactly one atom. Each atom within the original block is assigned to exactly one auxiliary lattice point. Now at most four atoms must be considered as potential collision partners at any time.

Suppose that the ion beam is travelling primarily in the z-direction, as shown in Figure 3.9. Its path is constructed by the intersects with consecutive z-planes.

Given a typical nearest neighbour distance of about 2 Å and a typical impact parameter of around 0.5 Å, the ion is close enough to no more than one atom, which means only four lattice points need be considered.

Although it may seem restrictive to have to construct a rectangular auxiliary lattice, this has not been found to be a problem even for quite complex reconstructions [19].

3.3.7 Multiparameter Simulations

When evaluating hitting probabilities by the methods described above the majority of computational time goes into the calculation of the ion trajectories, whilst relatively little is used in evaluating the probabilities. When comparing simulations with experimental data it is often desirable to vary several parameters over a small range of values in order to determine the most appropriate model. This can be achieved in a relatively efficient manner by the realisation that the information regarding the equilibrium positions of the atoms and their thermal vibrations is hidden within the Gaussian distributions G_i. These distributions do not enter into the calculations until after the calculation of the ion trajectories. Therefore one set of ion trajectories may be used to determine the hitting probabilities for a range a slightly different equilibrium positions and thermal vibrations of the atoms without significant increase in computational time. A range of structural models may then be simulated in a so called "multicalc", systematically varying atomic positions and/or vibrations between each model. This greatly accelerates the search for a structural solution, though care must be taken to ensure that parameters are not moved from the starting positions by too extreme an amount and that a sufficiently high number of ions are used. Experience has shown that an atomic shift of no more than ± 0.3 Å and an ingoing/outgoing ion flux of 100000/50000 ions is adequate in most situations.

3.4 Comparison of Simulation with Experimental Data

Angular cross sections through MEIS spectra produce a plot of scattering yield against scattering angle. Geometrical considerations may gave rise to a number of possible trial structures which are then simulated using the VEGAS code implementing the methods described above. The experimental cross sections are corrected for the effects of the Rutherford scattering cross section and the kinematic energy loss factor. The data may also be corrected for angular miscalibration of the TEA position by comparison of bulk blocking features to simulations of scattering from the bulk atoms of the crystal.

Experimental and simulated scattering curves are compared by use of an R-factor. The R-factor which has become standard within the Daresbury community is a chi-squared R-factor

$$R_{\chi} = \frac{1}{N}\sum_{n=1}^{N}\frac{(Y_n^{sim} - Y_n^{exp})^2}{Y_n^{exp}} \qquad (3.24)$$

Y^{exp} and Y^{sim} being the experimental and simulated yields and N the total number of points. A series of macros are available for the Igor Pro [24] software package [25] to perform such comparisons. As there is no calibration of the data to give absolute yields, the experimental data must be empirically scaled to the simulation. Values of R_{χ} obtained are therefore purely relative and cannot be compared with those obtained from other data sets or other scattering geometries. A further discussion of R-factors, including some problems associated with R_{χ}, may be found in Chapter 5.

References

1. W. C. Turkenburg, W. Soszka, F. W. Saris, H. H. Kersten and B. G. Colenbrander, *Nuc. Instrum. Meth.* **132** 587 (1976)

2. R. M. Tromp, *Medium Energy Ion Scattering*, in *Practical Surface Analysis*, p. 577, D. Briggs & M. P. Seah, (Eds.) John Wiley & Sons (1992)

3. J. F. van der Veen, *Surf. Sci. Rep.* **5** 199 (1985)

4. P. Quinn, D. Brown, D. P. Woodruff, T. C. Q. Noakes and P. Bailey, *Surf. Sci.* **491** 208 (2001)

5. P. Bailey, T. C. Q. Noakes and D. P. Woodruff, *Surf. Sci.* **426** 358 (1999)

6. D. Brown, T. C. Q. Noakes, D. P. Woodruff, P. Bailey and Y. Le Goaziou, *J. Phys. Condens. Matter* **11** 1889 (1999)

7. D. Brown, P. D. Quinn, D. P. Woodruff, T. C. Q. Noakes and P. Bailey, *Surf. Sci.* **497** 1 (2002)

8. P. Fenter and T. Gustafsson, *Phys. Rev. B* **38** 10197 (1988)

9. D. P. Woodruff, D. Brown, P. D. Quinn, T. C. Q. Noakes and P. Bailey, *Nucl. Instrum. Meth. B* **183** 128 (2001)

10. T. Yasue and T. Koshikawa, *Surf. Sci.* **377-379** 923 (1997)

11. M. Chester and T. Gustafsson, *Surf. Sci.* **256** 135 (1991)

12. M. Copel, T. Gustafsson, W. R. Graham and S. M. Yalisove, *Phys. Rev. B* **33** 8110 (1986)

13. B. W. Busche and T. Gustafsson, *Phys. Rev. B* **61** 16097 (2000)

14. S. M. Yalisove, W. R. Graham, E. D. Adams, M. Copel and T. Gustafsson, *Surf. Sci.* **171** 400 (1986)

15. T. Nishimura, A. Ikeda, H. Namba and Y. Kido, *Surf. Sci.* **411** L834 (1998)

16. R. L. Headrick and W. R. Graham, *Phys. Rev. B* **37** 1051 (1988)

17. J. V. Barth and D. E. Fowler, *Phys. Rev. B* **55** 1528 (1995)

18. P. Haberle and T. Gustafsson, *Phys. Rev. B* **40** 8218 (1989)

19. J. W. M. Frenken, R. M. Tromp and J. F. van der Veen, *Nucl. Instrum. Meth. B* **17** 334 (1986)

20. I. Stensgaard, R. Feidenhans'l and J. E. Sorensen, *Surf. Sci.* **128** 281 (1983)

21. R. M. Tromp and J. F. van der Veen, *Surf. Sci.* **133** 159 (1983)

22. VEGAS, *FOM Institute*

23. J. H. Barrett, *Phys. Rev. B* **3** 1527 (1973)

24. Igor Pro, *WaveMetrics Inc.*

25. Igor Pro MEIS Macros, P. Bailey, *Daresbury MEIS Facility*